# Understanding symptomatology of atherosclerotic plaque by image-based tissue characterization

U. Rajendra Acharya [a,b], Oliver Faust [c,*], Vinitha Sree S. [d], A.P.C. Alvin [a],
Ganapathy Krishnamurthi [e], José C.R. Seabra [f], João Sanches [f], Jasjit S. Suri [g,h]

[a] Department of Electrical and Computer Engineering, Ann Polytechnic, Singapore 599489, Singapore
[b] Department of Biomedical Engineering, Faculty of Engineering, University of Malaya, Malaysia
[c] Aberdeen University, Aberdeen, Scotland AB24 3FX, UK
[d] Global Biomedical Technologies Inc., CA, USA
[e] Case Western Reserve University in Cleveland, OH, USA
[f] Department of Electrical and Computer Engineering, Instituto Superior Técnico, Portugal
[g] Fellow AIMBE, CTO, Department of Diagnostic and Monitoring Division, AtheroPoint, LLC, Roseville, CA 95661, USA
[h] Idaho State University (Aff.), ID, USA

## ARTICLE INFO

## ABSTRACT

Characterization of carotid atherosclerosis and classification into either symptomatic or asymptomatic is crucial in terms of diagnosis and treatment planning for a range of cardiovascular diseases. This paper presents a computer-aided diagnosis (CAD) system (Atheromatic) that analyzes ultrasound images and classifies them into symptomatic and asymptomatic. The classification result is based on a combination of discrete wavelet transform, higher order spectra (HOS) and textural features. In this study, we compare support vector machine (SVM) classifiers with different kernels. The classifier with a radial basis function (RBF) kernel achieved an average accuracy of 91.7% as well as a sensitivity of 97%, and specificity of 80%. Thus, it is evident that the selected features and the classifier combination can efficiently categorize plaques into symptomatic and asymptomatic classes. Moreover, a novel symptomatic asymptomatic carotid index (SACI), which is an integrated index that is based on the significant features, has been proposed in this work. Each analyzed ultrasound image yields on SACI number. A high SACI value indicates that the image shows symptomatic and low value indicates asymptomatic plaques. We hope this SACI can support vascular surgeons during routine screening for asymptomatic plaques.

© 2012 Elsevier Ireland Ltd. All rights reserved.

## 1. Introduction

Atherosclerosis and high blood pressure are the main causes for heart disease and stroke [1]. Stroke ranks third among the most common cause of death in the majority of industrialized countries. Therefore, atherosclerosis is a real problem.

Stroke most commonly results from occlusion of a major artery in the brain and typically leads to the death of all cells within the affected tissue [2]. A major cause of this occlusion is atherosclerosis in the carotid artery. Atherosclerosis is a condition which leads to a thickening of arteries caused by plaque deposition [3]. It has been shown that the risk of ipsilateral stroke can be reduced by surgical removal of

plaques [4]. Since most of the carotid plaques are not harmful and since carotid surgery and stenting procedures have risks associated, there is a need for an adjunct modality that can aid the vascular surgeons to select with high confidence only those patients that definitely need the surgery. Based on autopsy analysis and ultrasound studies [5–8], it is known that both presence and extent of atherosclerotic lesions in a localized observation area correlate with atherosclerosis present in other parts of the circulatory system, e.g. coronary arteries.

The two crucial diagnostic steps for treatment planning and surgery include (1) detection of plaque and (2) the categorization of the plaque into symptomatic [9] or asymptomatic [10] classes. Researchers have proposed a range of methods for these purposes. Studies indicate that intravascular ultrasound measurement of coronary plaque volume is a good indicator for the efficacy of plaque related surgery and therapy. Unfortunately, intravascular ultrasound is invasive, potentially risky, and very expensive [11,12]. Non-invasive carotid artery ultrasound is another well-established visualization tool. It helps physicians to quantify atherosclerotic lesions. Medical specialists use this method to evaluate atherosclerotic disease in its early and advanced stages. This technique has also been used in many recent epidemiological studies and in atherosclerosis prevention trials. Moreover, studies using B-mode ultrasound for plaque morphology characterization suggest that this method is useful in assessing the vulnerability of atherosclerotic lesions [13–15], in spite of the non-availability of a way to classify risky plaques with adequate confidence and reproducibility. Despite these advantages and popular use, ultrasound has its own limitations. Due to low spatial resolution and artifacts, the correlation between features seen on the ultrasound images and those found in the histological examination of the plaques is not good [16,17]. Therefore, in order to increase this correlation between classification and histological results, there is a need for developing pre-processing techniques that improve the ultrasound image quality and for extracting discriminate features.

In this paper, we present an efficient plaque categorization algorithm that is based on several features extracted from B-mode ultrasound images. We call the system Atheromatic. The block diagram, in Fig. 1, shows the algorithm structure. The obtained B-mode ultrasound images are pre-processed, and image features based on the texture, Higher Order Spectra (HOS), and Discrete Wavelet Transform (DWT) are extracted. These features are then fed to the Support Vector Machine (SVM) classifier. The quality of these features led us to propose a new index which indicates whether or not a plaque formation is Amaurosis Fugax (AF) or asymptomatic (AS). Analysis shows that the proposed index is clinically significant.

This paper is organized as follows. In Section 2, we present the data collection procedure and describe the nature of the data. We also present the pre-processing steps employed. Subsequently, brief descriptions of the features are given. The SVM classifier is then presented. Furthermore, we explain the statistical tests which were used in this work. Section 3 presents the range of selected features and classification results. We also report on the symptomatic asymptomatic carotid index (SACI) parameter. In Section 4, we discuss a few related studies and compare them with our results. We conclude the paper in Section 5.

## 2. Materials and methods

This section introduces all materials and methods used in the proposed system. We organized the text in such a way that it reflects the structure of the block diagram which is shown in Fig. 1. In Section 2.1 both acquisition and preprocessing of carotid B-mode Ultrasound images are discussed. In Sections 2.2–2.5, we briefly describe the texture, DWT, and HOS feature extraction methodologies. The extracted features are analyzed with the so-called t-test. The t-test itself is introduced as part of the statistical analysis methods in Section 2.7. Finally, we discuss the SVM algorithm with different kernel configurations.

### 2.1. Carotid ultrasound image acquisition and preprocessing

The data was taken from 146 carotid bifurcation plaques in 99 patients, 75 males and 24 females. Mean age was 68 years old (41–88). Patients were observed consecutively through neurological consultation which included non-invasive examination with color-flow duplex scan of one or both carotids. A plaque was considered symptomatic when Amaurosis fugax or focal transitory, reversible or established neurological symptoms in the ipsilateral carotid territory, were observed in the previous 6 months. 102 plaques were identified as asymptomatic while 44 have shown symptoms.

Image normalization is an important step to guarantee that images acquired under different conditions yield comparable and reproducible features and classification results. Image normalization was achieved as previously reported [18]; hence, the image intensities were linearly scaled so that the adventitia and blood intensities would be in the range of 190–195 and 0–5, respectively.

The normalized image is used to segment existing plaque(s) in the image. Each plaque is delineated by drawing around its structure and the obtained contour is evenly resampled and smoothed using spline interpolation. De-speckled and Speckle images, needed to compute the echo-morphology and texture features, are computed from the normalized BUS images. In a first step, the eRF image is estimated from the normalized BUS according to [19]. In a second step, the estimated eRF image is used to compute the speckle-free and speckle components. This second step uses a Bayesian framework with the Maximum a Posteriori (MAP) criterion where the pixels are considered independent random variables with Rayleigh distribution, as described in [20].

### 2.2. Texture features

The three major goals of texture research are to understand, model and process texture. Ultimately, the aim is to simulate human visual learning processes using computer technology. Texture is defined as a regular repetition of an element or pattern in a surface structure [21]. Structural analysis and statistical analysis methods are the most commonly
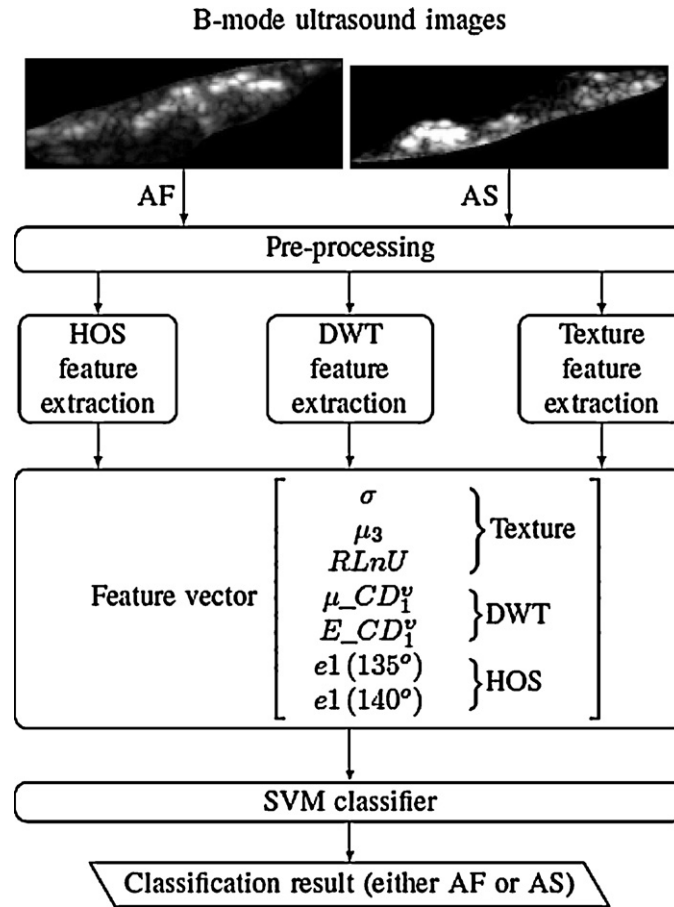
## B-mode ultrasound images



**Fig. 1 – Block diagram of the proposed system.**

used approaches to analyze the texture of an image. In the case of the statistical approach, the distribution of the pixel intensities and the relationships between the intensities are analyzed. In this work, we have used the statistical analysis method, namely, the gray level co-occurrence matrix (GLCM), to extract the third moment feature. Structural texture analysis is more complex when compared to the statistical approach [22], because it studies the symbolic descriptions of the image. It has been found that the statistical approach based features are more useful for analysis than the structural features [23]. We have used the statistical analysis method called run length matrix to extract the run length non-uniformity (RLnU) feature. The remainder of this section briefly explains the different statistical features extracted from the carotid ultrasound images.

Let $\phi(i)$ for $i = 1, 2, \ldots, n$ be the number of points whose intensity is $i$ in the image and A1 be the area of the image. The occurrence probability of intensity in the image is defined as:

$$h(i) = \frac{\varphi(i)}{A1} \tag{1}$$

The standard deviation is given by:

$$\sigma = \sum_{i=0}^{n} (i - \mu)^2 h(i) \tag{2}$$

where $\sigma$ is the deviation and $\mu$ is the mean of intensities.

1. Co-occurrence matrix: the GLCM of a $m \times n$ image I is defined [24] as:

$$C_d = |\{(p, \quad q), \quad (p + \Delta x, \quad q + \Delta y) : I(p, \quad q) = i, \quad I(p + \Delta x, q + \Delta y) = j\}| \tag{3}$$ where $(p, q)$, $(p + \Delta x, q + \Delta y)$ belongs to a $m \times n$, $d = (\Delta x, \Delta y)$ and $|\cdot|$ denotes the set cardinality. The probability of a pixel with a gray level value $i$ having a pixel with a gray level value $j$ at a distance $(\Delta x, \Delta y)$ away in an image is:

$$P_d(i, j) = \frac{C_d(i, j)}{\sum_{\langle i \rangle} \sum_{\langle j \rangle} C_d(i, j)} \tag{4}$$

where the summation is over all possible i, Based on the GLCM, we obtain the *Third_moment* as:

$$Third\_moment = -\sum_{\langle i \rangle} \sum_{\langle j \rangle} (i - j)^3 P_d(i, j) \tag{5}$$

2. *Run Length non uniformity* (RLnU): The run length matrix $P_\theta$ contains all the elements where the gray level value $i$ has the run length $j$ continuous in direction $\theta$ [25]. Often the
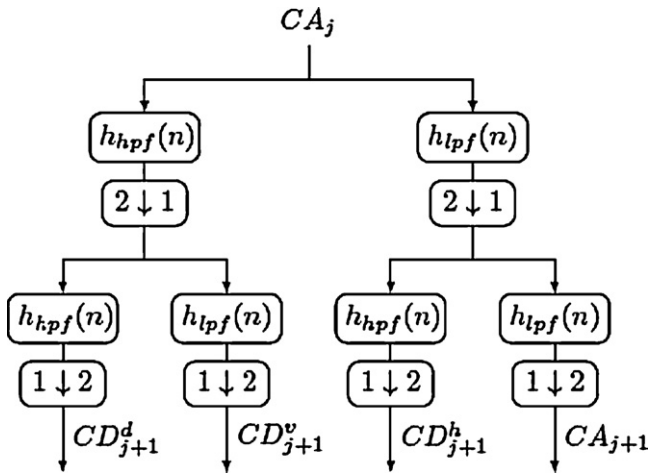
**Fig. 2 – Two-dimensional DWT where 2↓1 indicates down sampling the columns by 2 and 1↓2 indicates down sampling the rows by 2.**

direction $\theta$ is set as 0°, 45°, 90°, or 135° ... $RLnU$ is defined as [26]:

$$RLnU = \sum_{\langle j \rangle} \left( \sum_{\langle i \rangle} P_\theta(i,j) \right)^2 \tag{6}$$

The $RLnU$ measures the similarity of the length of runs throughout the image. The value is expected to be small if the run lengths are alike throughout the image.

### 2.3. Discrete wavelet transform features

In both numerical and functional analysis, a DWT is any wavelet transform for which the wavelets are discretely sampled [27]. A key advantage over the well-known Fourier transforms [28] is temporal resolution: it captures both frequency and location information (position in time).

The two-dimensional DWT leads to a decomposition of approximation coefficients at level $j$ in four components: the approximation $CA_{j+1}$ at level $j+1$, and the details in three orientations (horizontal $CD^h_{j+1}$, vertical $CD^v_{j+1}$, and diagonal $CD^d_{j+1}$). Fig. 2 describes the basic decomposition steps for images.

In this work we have used Biorthogonal 3.1 wavelet. The properties are symmetric, not orthogonal and biorthogonal. Fig. 3 shows the coefficients for both decomposition low and high pass filters for this wavelet.

We have used the average intensity of $CD^v_1$ as the first DWT feature:

$$AVERAGE\_CD^v_1 = \sum_{\langle j \rangle} \sum_{\langle i \rangle} CD^v_1(i,j) \tag{7}$$

The second DWT feature was defined as the energy of $CD^v_1$.

$$AVERAGE\_CD^v_1 = \sum_{\langle j \rangle} \sum_{\langle i \rangle} (CD^v_1(i,j))^2 \tag{8}$$
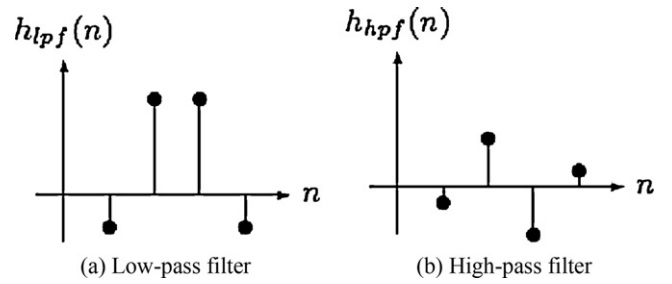


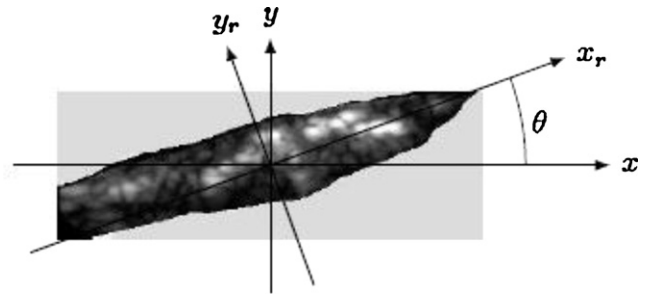**Fig. 3 – (a and b) Biorthogonal 3.1 decomposition filter.**



**Fig. 4 – Geometry of Radon transform.**

### 2.4. Radon transform

The Radon transform is widely used in image processing for handling medical images [29]. The algorithm computes line integrals along many parallel beams or paths in an image from different angles $\theta$ by rotating the image around its centre. This transforms the image pixel intensity values along these lines into points in the Radon domain.

The Radon transform of $f(x, y)$ is the line integral of $f$ parallel to the $y_r$-axis and is given by

$$R_\theta = \int_{-\infty}^{\infty} f(x_r, y_r) \, dy_r \tag{9}$$

where

$$\begin{bmatrix} x_r \\ y_r \end{bmatrix} = \begin{bmatrix} \cos(\theta) & \sin(\theta) \\ -\sin(\theta) & \cos(\theta) \end{bmatrix} \begin{bmatrix} x \\ y \end{bmatrix} \tag{10}$$

Thus the radon transform converts 2D image into 1D parallel beam projections at various angles, and in this work, we have used a step size of $\theta = 5°$. The geometry of the Radon transform is illustrated in Fig. 4.

### 2.5. Higher order spectra (HOS)

The entropy features obtained from the Bi-spectrum are used in this work. The Bi-spectrum is a complex valued function of two frequencies given by

$$B(f_1, f_2) = E[A(f_1)X(f_2) * X(f_2 + f_2)] \tag{11}$$

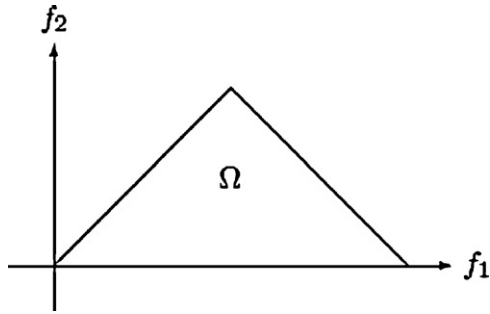where $X(f)$ is the Fourier transform of the signal $x(nT)$.

**Fig. 5 – Non-redundant region for the computation of the Bi-spectrum for real signals. Parameters are calculated in the region $\Omega$.**

The frequency $f$ maybe normalized by Nyquist frequency so as to be between 0 and 1. The Bi-spectrum, which is the product of the three Fourier coefficients, exhibits symmetry, and is computed to the non-redundant region. This is termed as $\Omega$, the principal domain or the non-redundant region (i.e. the triangle region in Fig. 5). Bi-spectrum phase entropy [30–32] is defined as:

$$e1 = \sum_n p(\psi_n) \; \log(\psi_n)$$

$$p(\psi_n) = \frac{1}{L} \sum_\Omega l(\varphi(B(f1, f2) \in \psi_n)$$

$$(12)$$

$$\psi_n = \left\{ \varphi | -\pi + \frac{2\pi n}{N} \leq \varphi < -\pi + \frac{2\pi(n+1)}{N} \right\}$$

$$n = 0, 1, \ldots, N-1$$

$$(13)$$

where $L$ is the number of points within the region $\Omega$ in Fig. 5, $\varphi$ refers to the phase angle of the bi-spectrum, and $l(\cdot)$ is an indicator function which gives a value of l when the phase angle is within the range of $\psi_n$ given in Eq. (13).

In this study we have used the phase entropy on the radon transform for $\theta = 135°$ and $\theta = 140°$ of the B-mode ultrasound images. This yields two features: $e1(135°)$ and $e1(140°)$.

## 2.6. Classification using support vector machines (SVM)

The SVM is a maximum margin classifier, i.e. it maximizes the distance between the decision hyperplane and the closest class training data called support vectors. Initially designed for two class problems, it has been extended for multiclass as well. We describe below the SVM method:

Consider two class classifications using a linear model of the form

$$y(x) = w^T \phi(x) + b$$

$$(14)$$

where $\varphi(x)$ denotes the feature transformation kernel, $b$ the bias parameter. The vector $w$ is normal to the hyper-plane. The training data consists of the input feature vectors $x$ and the corresponding classes $c$ (−1 or 1). The new feature vectors are classified according to the sign of $y$.

The margin is given by the perpendicular distance to the closest point $x$ from the training data set. The goal is to find the maximum margin hyper-plane while at the same time assigning a soft penalty to points that are on the wrong side of the margin. The problem is then to minimize,

$$C \sum_{i=1}^N \xi_i + \frac{1}{2} ||w||^2$$
$$c_i y(x_i) \geq 1 - \xi_i, \quad \xi \geq 0$$

$$(15)$$

where $\xi_I$ are penalty terms for points that are misclassified. The first term is equivalent to maximizing the margin and $C$ is the regularization parameter that controls the tradeoff between the misclassified points and the margin.

This quadratic programming problem is solved by introducing Lagrange multipliers $a_n$ for each of the constraints and solving the dual formulation. The Lagrangian is given by

$$L(w, b, a) = \frac{1}{2} ||w||^2 + C \sum_{i=1}^N \xi_i - \sum_{i=1}^N a_i[c_i y(x_i) - 1 + \xi_i] - \sum_{i=1}^N \mu_i \xi_i \quad (16)$$

where $a_i$ and $\mu_i$ are the Lagrange multipliers. After eliminating $w$, $b$ and $\xi_I$ from the Lagrangian we obtain the dual Lagrangian which we maximize.

$$\tilde{L}(a) = \sum_{i=1}^N a_i - \frac{1}{2} \sum_{i=1}^N \sum_{j=1}^N a_i a_j c_i c_j k(x_i, x_j)$$
$$k(x_i, x_j) = \phi(x_i)^T \cdot \phi(x_j)$$

$$(17)$$

$$0 \leq a_n \leq C, \quad \sum_{i=1}^N a_i c_i = 0$$

The predictive model is given by

$$y(x) = \sum_{i=1}^N a_i c_i k(x, x_i) + b$$

$$(18)$$

and $b$ is estimated by

$$b = \frac{1}{N_M} \sum_{i \in M} \left( c_i - \sum_{j \in S} a_j c_j k(x_i, x_j) \right)$$

$$(19)$$

$M$ is the set of indices such that $0 < a_i < C$.

A solution to the quadratic programming problem of maximizing the dual Lagrangian (17) is given in [33]. The original SVM algorithm was a linear classifier. However, Boser et al. [34] suggested a way to create non-linear classifiers by applying a different kernel to maximum-margin hyper-planes. The method of using a different kernel in this type of arrangement was originally proposed by Aizerman et al. [35]. The resulting algorithm is similar to the original SVM algorithm, except that every dot product is replaced by a nonlinear kernel function as shown in (17). This allows the algorithm to fit the maximum-margin hyper-plane in a transformed feature space.

Five standard kernels were used for classification. The linear kernel, polynomial kernel of order 1, 2 and 3 and the Radial

**Table 1 – t-Test results for DWT, HOS and texture features.**

| Features | Symptomatic | Asymptomatic | P value |
|---|---|---|---|
| $\sigma$ | $32.8 \pm 9.57$ | $37.9 \pm 11.0$ | 0.0046 |
| $\mu_s$ | $2.93 \pm 1.32$ | $2.39 \pm 0.98$ | 0.0047 |
| RLnU | $4.083E+03 \pm 1.114E+03$ | $2.653E+03 \pm 546$ | <0.0001 |
| $\mu\_CD_1^v$ | $5.034E-02 \pm 1.248E-02$ | $4.477E-02 \pm 1.140E-02$ | 0.0060 |
| $E\_CD_1^v$ | $6.500E-08 \pm 1.695E-08$ | $5.758E-08 \pm 1.579E-08$ | 0.0078 |
| e1(135°) | $1.59 \pm 0.536$ | $2.04 \pm 0.644$ | <0.0001 |
| e1(140°) | $1.18 \pm 0.399$ | $1.56 \pm 0.732$ | 0.0008 |

**Table 2 – Classification results where TN is true negative, FN is false negative, TP is true positive, and FP is false positive.**

| SVM | TN | FN | TP | FP | Accuracy | PPV | Sensitivity | Specificity | AUC |
|---|---|---|---|---|---|---|---|---|---|
| Linear Kernel | 12 | 2 | 31 | 3 | 89.6% | 90.7% | 94.9% | 77.8% | 0.870 |
| Polynomial Kernel with order 2 | 12 | 2 | 31 | 3 | 89.6% | 91.6% | 93.9% | 80% | 0.870 |
| Polynomial Kernel with order 3 | 12 | 3 | 30 | 3 | 86.1% | 90.8% | 89.9% | 77.8% | 0.855 |
| RBF Kernel | 12 | 1 | 32 | 3 | 91.7% | 91.8% | 97% | 80% | 0.885 |

Basis Function Kernel were used. The polynomial kernel is defined as

$$k(x_i, x_j) = (1 + x_i.x_j)^p \tag{20}$$

where $p$ is the order of the kernel and the RBF kernel is defined as

$$k(x_i, x_j) = \exp\left(-||x_i - x_j||^2\right) \tag{21}$$

### 2.7. Statistical analysis

The $t$-test is a statistical test used to determine if the means of two features in two classes are different [36]. The probability of rejecting the null hypothesis that the means are the same (with an assumption of a true null hypothesis) is given by the $p$-value. If the $p$-value is low (less than 0.05 or 0.01), then it indicates that the null hypothesis is false, and therefore, the features are significantly different for the two classes.

The receiver operating characteristic (ROC) is a two-dimensional plot with (100-specificity) on the $x$-axis and (sensitivity) on the $y$-axis. These values are calculated for a range of cut-off points, and plotted to get the ROC curve. The area under the ROC curve (AUC) is used to determine the quality of the classifiers. AUC is between 0.5 and 1, and the better the classifier is, the closer is the AUC to unity [37]. AUC has been reported to be a good classifier performance measure [38].

## 3. Results

Threefold stratified cross validation was used for data resampling [39]. Two-thirds of the data were used for training and the remaining one-third was used to test the performance. This procedure was repeated three times using different folds of the test data each time. Subsequently, we calculated the accuracy, sensitivity, specificity, positive predictive value (PPV), and AUC by averaging the values obtained in three iterations.

### 3.1. Statistical results

Table 1 presents the significant HOS, texture, and DWT features that were extracted from the ultrasound images using

techniques described in the previous section. The significant features, their respective range (mean ± standard deviation) for both classes, and the $p$-values are shown in the table. It is evident that all the seven features have a $p$-value less than 0.01, and hence, these features can be considered significant enough for classification.

### 3.2. SVM results

The performance measures (sensitivity, specificity, accuracy, and AUC values) obtained using the selected features to evaluate different SVM kernel functions are shown in Table 2. It can be seen that the SVM classifier with the RBF kernel presented the highest performance measures (Accuracy: 91.7%; Sensitivity: 97%; Specificity: 80%; AUC: 0.885) among all the other SVM configurations. The ROC curves obtained for all SVM configurations are depicted in Fig. 6. As seen from the ROC curves, the SVM classifier with the RBF kernel function is the better classifier amongst the rest as it has the highest AUC of 0.885.

### 3.3. Index results

We have shown how well the seven features differentiate symptomatic and asymptomatic plaque formations in B-mode ultrasound images. However, keeping continuous track of the variations in these seven features in a patient in order to make a diagnosis is a time-consuming and difficult task that is prone to human errors. Hence, we integrated the features in such a way that the index value for symptomatic is distinctly different from the value resulting from asymptomatic plaque formations. This novel integrated index, termed Symptomatic Asymptomatic Carotid Index (SACI), is defined as

$$SACI = 2 \log_{10}(RLnU) - \frac{\log_{10}(R1 - R2 * R3)}{5}$$

$$R1 = \log_{10}\left(\frac{AVERAGE\_CD_1^v}{ENERGY\_CD_1^V}\right) \tag{22}$$

$$R2 = Deviation \times Third\_Moment$$

$$R3 = e1(135°) \times e1(140°)$$

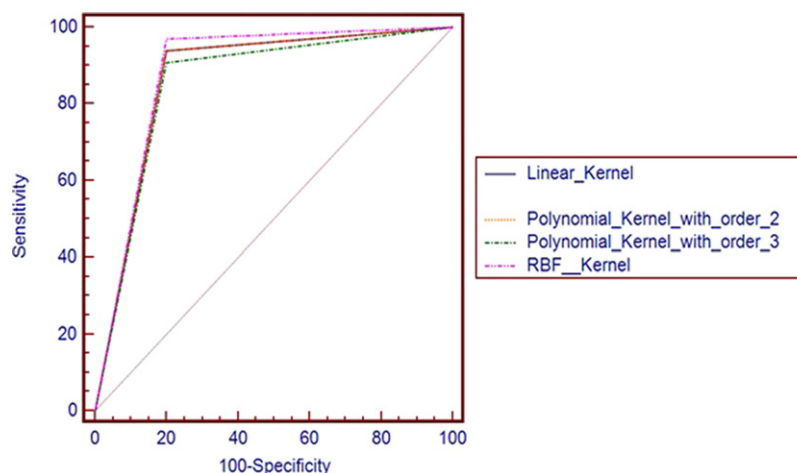Table 3 shows mean and variance of SACI for symptomatic and asymptomatic carotid ultrasound images. The $p$-value is

Fig. 6 – ROC curves for the different SVM kernels.

**Table 3 – Range of index values for symptomatic and asymptomatic.**

| Feature | Symptomatic | Asymptomatic | P value |
|---------|-------------|--------------|---------|
| Index | $7.04 \pm 0.223$ | $6.67 \pm 0.186$ | <0.0001 |

very low (<0.0001), therefore these values are clinically significant. The distribution of the SACI for symptomatic and symptomatic classes is distinct as shown in the box-plot (Fig. 7).
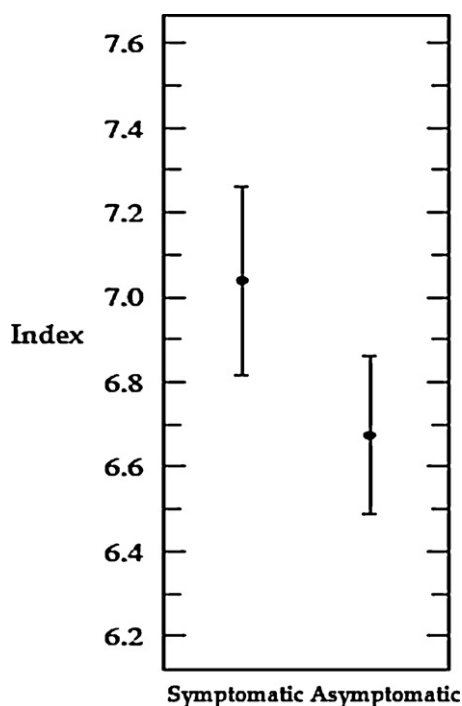


Fig. 7 – Box plot of the SACI index.

## 4. Discussion

In this section, we discuss the background of carotid ultrasound imaging and plaque identification. The discussion starts with tissue-mimicking phantoms which are very useful in the field of plaque characterization, because the phantoms help to test ultrasound equipment under controlled conditions. The base assumption behind these tissue mimicking phantoms is that carotid plaques are characterized by a lipid-rich core with abundant inflammatory cells and a thin fibrous cap. The aim of the phantoms is to mimic this scenario as close as possible.

Balocco et al. presented an indirect approach to estimating the mechanical properties of tissues surrounding the arterial vessels using ultrasound Doppler measurements combined with an inverse problem solving method [40]. The phantom measurement results showed good correlation with theoretical values. A study by Fromageau et al. is dedicated to the characterization of polyvinyl alcohol cryogel (PVA-C) for these types of applications [41]. For the samples that underwent less than seven freeze–thaw cycles, the Young's moduli estimated with the four elastography methods showed good matching with the mechanical tensile tests with a regression coefficient varying from 0.97 to 1.07, and correlations R2 varying from 0.93 to 0.99, depending on the method. Thermal strain imaging using intravascular ultrasound have been proposed for high-risk arterial plaque detection, in which image contrast results from the temperature dependence of sound speed. Yan et al. see a potential to distinguish a lipid-laden lesion from the arterial vascular wall due to its strong contrast between water-bearing and lipid-bearing tissue. Initial simulations and phantom experiments indicate plaque identification is possible for a 176° temperature rise [42].

These tissue mimicking phantoms deliver a practical justification for the discriminative ability of B-mode carotid ultrasound images. The discriminative abilities have been used by a number of projects which were concerned with plaque image analyses. This analysis is a real practical application because it helps to assess the risk of stroke and other cardiovascular diseases and thereby, such systems support

disease diagnosis. Kyriacou et al. discuss several plaque-image analysis methods that have been developed over the past years [43]. They review of clinical methods for visual classification that have led to standardized methods for image acquisition and describe methods for image segmentation and de-noising.

Kyriacou et al. (2005) evaluated the efficacy of computer aided diagnosis based on neural and statistical classifiers using texture and morphological features [44]. In their study they used several classifiers like the K-Nearest Neighbour, the Probabilistic Neural Network and the SVM. As result they report a diagnostic accuracy up to 71.2%. Kyriacou et al. (2009) studied the usefulness of multilevel binary and gray scale morphological analysis in the assessment of atherosclerotic carotid plaques [45]. With their method they extracted pattern spectra from ultrasound images which were used as classification features. SVM and probabilistic neural network were used for classifying the features into either a symptomatic or an asymptomatic class. The classification accuracy was 73.7% for multilevel binary morphological image analysis and 66.8% for gray scale morphological analysis. Both were achieved using the SVM classifier.

Recently, Seabra et al. [46] proposed a method for plaque characterization based on a de-speckling algorithm, resulting in features extracted from de-speckled and speckle image sources. In this study, the use of textural information for correct identification of different plaque types was reinforced. They obtained an almost perfect classification result in terms of sensitivity and accuracy. They use a combination of clinical information based features like degree of stenosis, evidence of plaque disruption, etc. along with texture features, DWT and other features giving a total of 114 features per image. They use an Adaboost (Adaptive Boosting) classifier with decision stumps. A direct comparison with their results is not possible because of the difference in the feature space. However, they do show a sensitivity of 90% when using only texture and histogram features computed from normalized BUS images which is comparable to our results. We were able to achieve 89% sensitivity based on a limited number of features extracted automatically.

Tissue mimicking phantoms help us to improve the ultrasound scanning process. More sophisticated image processing and feature extraction methods yield more discriminative features. Both, improvements in the scanning process and in the signal processing are necessary to achieve higher classification accuracies. With current technology, our system can diagnose two types of plaque formations with an accuracy of around 90%. These results were achieved under lab conditions, and therefore, it is expected that the accuracy goes down when these methods are employed in a system used in a medical work flow. Therefore, more research is necessary to further improve the classification accuracy.

In our earlier study [47], we used only the texture features (standard deviation, entropy, symmetry, and run percentage) in Adaboost and SVM classifiers. SVM with radial basis function kernel resulted in the highest classification accuracy of 82.4%. Recently, averaged DWT coefficients fed to the SVM classifier were able to diagnose the two classes automatically with an accuracy of 83.7%, sensitivity of 80%, and specificity of 86.4% [48]. We believed that the classifier performance

could be improved with the addition of more relevant features. Therefore, in this study, we used DWT and HOS features in addition to the texture features and obtained an improved accuracy of 91.7%.

Our preliminary results suggest that HOS features are very powerful features that lead to improvement in classification. The entropy of the Bispectrum has been used to classify EEG signals [31,32]. We evaluated the usefulness of this feature by running the classifier without the Bi-spectrum entropy and we obtained an accuracy of 88.2%. Including the HOS features led to an increased accuracy of 91.7%. In addition, we also performed classification by leaving out one feature at a time. Leaving out the third moment and run length non-uniformity one at a time leads to a 10% drop in accuracy. Leaving out HOS features and run length non-uniformity leads to a 6% drop in accuracy. The run length non-uniformity measures the homogeneity of an image and the phase entropy of the bispectrum is yet another measure of texture. Table 1 suggests that they capture different aspects of texture features as the RnLU value is significantly higher and the HOS features values significantly lower for the symptomatic. These results confirm that texture features are important for accurate classification of Carotid plaque images.

The AUC shows that the RBF kernel gives the best performance. The RBF kernel can be expanded in to an infinite series giving rise to an infinite dimensional polynomial kernel. Each of these polynomial kernels can then transform certain dimensions to make them linearly independent. It is then expected that the RBF kernel would work better than the linear or the polynomial kernel. We can also expect the polynomial kernels and the linear kernel to have the same performance as they both transform the feature space into a higher dimensional space where they are expected to be linearly separable by considering combinations of the feature vectors. In the case of polynomial kernel, the performance depends on the order of the polynomial. The SACI values (Table 3) show a significant difference between asymptomatic and symptomatic groups. Unlike the classifier the SACI is a continuous index and it gives a quantitative measure of how symptomatic (or asymptomatic) a patient is based on all the features considered for the classifier.

The practical value of this system depends on the input data. In this paper, we show that it is possible to achieve a classification accuracy of 91.7%. This result was achieved with data which was new to the classification algorithms, i.e. an unknown test set. Hence, we are fairly sure that the system will perform in a practical setting, under the condition that the input data is similar to the data we have used in this study. However, our theoretical treatment of this classification problem does not take into account any practical problems, such as system errors, corrupted input data and result misinterpretations. These issues need to be addressed in a later stage of building such a plaque identification system.

## 5.    Conclusion

Plaque identification from B-mode ultrasound images is very a difficult task. In most cases, such a characterization is carried out by well trained ultrasonographers and physicians

who visually scan the acquired ultrasound image. This is a time-consuming tedious task that is prone to inter-observer variability. Moreover, in most cases, it is difficult to accurately capture and differentiate the plaque edges and blood. With the advent of computer programming methods, efforts are being continually made to make this entire process automated and more efficient. In a quest towards developing such a method, we have proposed a CAD technique that is based on using advanced DWT and texture features and HOS information (Bispectrum) in a SVM classifier to categorize the plaque into symptomatic and asymptomatic classes. We have also demonstrated that our technique has a good classification accuracy of around 92%. Thus, the proposed CAD system (Atheromatic) may be a valuable tool which helps to optimize the clinical work flow process by providing more decision support to the vascular surgeons in selecting patients for treatment. Furthermore, a novel, unique and single integrated index called the symptomatic asymptomatic carotid index has been proposed to identify the nature of the plaque using a single number in order to make the diagnosis more objective.

## REFERENCES

[1] D.R. Labarthe, Epidemiology and Prevention of Cardiovascular Diseases: A Global Challenge, An Aspen Publication, 1998.

[2] N.R. Sims, H. Muyderman, Mitochondria, oxidative metabolism and cell death in stroke, Biochimica et Biophysica Acta (BBA): Molecular Basis of Disease 1802 (1) (2010) 80–91, mitochondrial Dysfunction (online). Available at: http://www.sciencedirect.com/science/article/B6T1Y-4X6VMDV-3/2/abb3ed7126ab1e8e67035977a72d7425

[3] A. Maton, R.L.J. Hopkins, C.W. McLaughlin, S. Johnson, M.Q. Warner, D. LaHart, J.D. Wright, Human Biology and Health, Prentice Hall, Englewood Cliffs, New Jersey, USA, 1993.

[4] G.G. Ferguson, M. Eliasziw, H.W.K. Barr, G.P. Clagett, R.W. Barnes, M.C. Wallace, D.W. Taylor, R.B. Haynes, J.W. Finan, V.C. Hachinski, H.J.M. Barnett, The North American Symptomatic Carotid Endarterectomy Trial: surgical results in 1415 patients, Stroke 30 (9) (1999) 1751–1758 (online). Available at: http://stroke.ahajournals.org/cgi/content/abstract/30/9/1751

[5] L.A. Solberg, P.A. McGarry, J. Moossy, J.P. Strong, C. Tejada, A.C. Lken, Severity of atherosclerosis in cerebral arteries, coronary arteries, and aortas, Annals of the New York Academy of Sciences 149 (1968) 956–973.

[6] A.M. Pancioli, J. Broderick, R. Kothari, T. Brott, A. Tuchfarber, R. Miller, J. Khoury, E. Jauch, Public perception of stroke warning signs and knowledge of potential risk factors, Journal of American Medical Association 279 (16) (1998) 1288–1292 (online). Available at: http://jama.amaassn.org/cgi/content/abstract/279/16/1288

[7] T. Craven, J. Ryu, M. Espeland, F. Kahl, W. McKinney, J. Toole, M. McMahan, C. Thompson, G. Heiss, d.J.R. Crouse, Evaluation of the associations between carotid artery atherosclerosis and coronary artery stenosis. A case-control study, Circulation 82 (4) (1990), pp. 1242–1230 (online). Available at: http://circ.ahajournals.org/cgi/content/abstract/82/4/1230

[8] I. Kallikazaros, C. Tsioufis, S. Sideris, C. Stefanadis, P. Toutouzas, Carotid artery disease as a marker for the presence of severe coronary artery disease in patients evaluated for chest pain, Stroke 30 (5) (1999) 1002–1007

[9] J. Golledge, R.M. Greenhalgh, A.H. Davies, The symptomatic carotid plaque, Stroke 31 (3) (2000) 774–781 (online). Available: http://stroke.ahajournals.org/cgi/content/abstract/31/3/774

[10] J.M. Johnson, M.M. Kennelly, D. Decesare, S. Morgan, A. Sparrow, Natural history of asymptomatic carotid plaque, Archives of Surgery 120 (9) (1985) 1010–1012 (online). Available at: http://archsurg.ama-assn.org/cgi/content/abstract/120/9/1010

[11] S.E. Nissen, E.M. Tuzcu, P. Schoenhagen, B.G. Brown, P. Ganz, R.A. Vogel, T. Crowe, G. Howard, C.J. Cooper, B. Brodie, C.L. Grines, A.N. DeMaria, Effect of intensive compared with moderate lipid-lowering therapy on progression of coronary atherosclerosis: a randomized controlled trial, Journal of American Medical Association 291 (9) (2004) 1071–1080 (online). Available at: http://jama.amaassn.org/cgi/content/abstract/291/9/1071

[12] M.-L.M. Gronholdt, B.G. Nordestgaard, T.V. Schroeder, S. Vorstrup, H. Sillesen, Ultrasonic echolucent carotid plaques predict future strokes, Circulation 104 (1) (2001) 68–73 (online). Available at: http://circ.ahajournals.org/cgi/content/abstract/104/1/68

[13] A.F. AbuRahma, J. Wulu, T. John, B. Crotty, Carotid plaque ultrasonic heterogeneity and severity of stenosis, Stroke 33 (7) (2002) 1772–1775 (online). Available at: http://stroke.ahajournals.org/cgi/content/abstract/33/7/1772

[14] M.M. Sabetai, T.J. Tegos, A.N. Nicolaides, T.S. El-Atrozy, S. Dhanjil, M. Griffin, G. Belcaro, G. Geroulakos, Hemispheric symptoms and carotid plaque echomorphology, Journal of Vascular Surgery 31 (1) (2000) 39–49 (online). Available at: http://www.sciencedirect.com/science/article/B6WMJ-4HK02FR5/2/98804a69b9187775f7e163971f96b1a9

[15] T.S. Hatsukami, M.S. Ferguson, K.W. Beach, D. Gordon, P. Detmer, D. Burns, C. Alpers, D.E. Strandness, Carotid plaque morphology and clinical events, Stroke 28 (1) (1997) 95–100 (online). Available at: http://stroke.ahajournals.org/cgi/content/abstract/28/1/95

[16] D.W. Droste, M. Karl, R.M.K.M. Bohle, Comparison of ultrasonic and histopathological features of carotid artery stenosis, Neurological Research 19 (1997) 380–384.

[17] E. Ringelstein, C. Sievers, S. Ecker, P. Schneider, S. Otis, Noninvasive assessment of $CO_2$-induced cerebral vasomotor response in normal individuals and patients with internal carotid artery occlusions, Stroke 19 (8) (1988) 963–969 (online). Available at: http://stroke.ahajournals.org/cgi/content/abstract/19/8/963

[18] T. Elatrozy, A. Nicolaides, T. Tegos, M. Griffin, The objective characterisation of ultrasonic carotid plaque features, European Journal of Vascular and Endovascular Surgery 16 (3) (1998) 223–230 (online). Available at: http://www.sciencedirect.com/science/article/B6WF5-4H3SF3Y-8/2/8011fe8e92fdb924982dfc5442f916ba

[19] J. Seabra, J. Sanches, Modeling log-compressed ultrasound images for radio frequency signal recovery, in: Conference Proceedings of the IEEE Engineering in Medicine and Biology Society, 2008, pp. 426–429 (online). Available at: http://www.biomedsearch.com/nih/Modeling-logcompressed-ultrasound-images/19162684.html

[20] J. Seabra, J. Xavier, J. Sanches, Convex ultrasound image reconstruction with log-Euclidean priors, in: Conference Proceedings of the IEEE Engineering in Medicine and Biology Society, 2008, pp. 435–438.

[21] M. Mirmehdi, X. Xie, J. Suri, Handbook of Texture Analysis, Imperial College Press, London, UK, 2009.

[22] R.C. Gonzalez, R.E. Woods, Digital Image Processing, 3rd ed., Prentice-Hall Inc., Upper Saddle River, NJ, USA, 2006.

[23] G. Castellano, L. Bonilha, L.M. Li, F. Cendes, Texture analysis of medical images, Clinical Radiology 59 (12) (2004) 1061–1069 (online). Available at: http://www.biomedsearch.com/nih/Textureanalysis-medical-images/15556588.html

[24] J.-H. Tan, E. Ng, U.R. Acharya, C. Chee, Study of normal ocular thermogram using textural parameters, Infrared Physics & Technology 53 (2) (2010) 120–126 (online). Available at: http://www.sciencedirect.com/science/article/B6TJ9-4XHVH7B-1/2/a85528a996940bce2b3d6cbf608083bd

[25] M.M. Galloway, Texture analysis using grey level run lengths, NASA STI/Recon Technical Report N, vol. 75, 1974 July, pp. 18.

[26] D. Xu, A.S. Kurani, J.D. Furst, D.S. Raicu, Run-length encoding for volumetric texture, in: The 4th IASTED International Conference on Visualization, Imaging, and Image Processing, 2004.

[27] S. Mallat, A Wavelet Tour of Signal Processing The Sparse Way, 3rd ed., Academic Press, 2008.

[28] S. Bochner, K. Chandrasekharan, Fourier Transforms, ser. Ann. Math. Stud., Princeton University Press, Princeton, NJ, 1949.

[29] A. Ramm, A. Katsevich, The Radon Transform and Local Tomography, CRC Press, 1996 (online). Available at: http://books.google.com.sg/books?id=Ifce8tC7sagC

[30] K.C. Chua, V. Chandran, R. Acharya, C.M. Lim, Automatic Identification of Epilepsy by HOS and Power Spectrum Parameters Using EEG Signals: A Comparative Study, 2008 (online). Available at: http://eprints.qut.edu.au/14787/

[31] K. Chua, V. Chandran, U. Acharya, C. Lim, Application of higher order spectra to identify epileptic EEG, Journal of Medical Systems (2010) 1–9, 10.1007/s10916-010-9433-z (online). Available at: http://dx.doi.org/10.1007/s10916-010-9433-z

[32] U.R. Acharya, E.C.P. Chua, K.C. Chua, C.M. Lim, T. Tamura, Analysis and automatic identification of sleep stages using higher order spectra, International Journal of Neural Systems 20 (6) (2010) 509–521.

[33] C. Cortes, V. Vapnik, Support-vector networks, Machine Learning 20 (September) (1995) 273–297 (online). Available at: http://portal.acm.org/citation.cfm?id=218919.218929

[34] B.E. Boser, I.M. Guyon, V.N. Vapnik, A training algorithm for optimal margin classifiers, in: Proceedings of the Fifth Annual Workshop on Computational Learning Theory, Ser. COLT'92, ACM, New York, NY, USA, 1992, pp. 144–152 (online). Available at: http://doi.acm.org/10.1145/130385.130401

[35] M.A. Aizerman, E.A. Braverman, L. Rozonoer, Theoretical foundations of the potential function method in pattern recognition learning, Automation and Remote Control (25) (1964) 821–837.

[36] J.F. Box, Guinness, gosset, fisher, and small samples, Statistical Science 2 (1) (1987) 45–52.

[37] K.H. Zou, A.J. O'Malley, L. Mauri, Receiver-operating characteristic analysis for evaluating diagnostic tests and predictive models, Circulation 115 (5) (2007) 654–657 (online). Available at: http://circ.ahajournals.org

[38] T.J.J. Downey, D.J. Meyer, R.K. Price, E.L. Spitznagel, Using the receiver operating characteristic to assess the performance of neural classifiers, in: International Joint Conference on Neural Networks (IJCNN'99), 1999, pp. 3642–3646.

[39] R. Kohavi, A study of cross-validation and bootstrap for accuracy estimation and model selection, in: Proceedings of the 14th International Joint Conference on Artificial intelligence, vol. 2, Morgan Kaufmann Publishers Inc., San Francisco, CA, USA, 1995, pp. 1137–1143 (online). Available at: http://portal.acm.org/citation.cfm?id=1643031.1643047

[40] S. Balocco, O. Basset, G. Courbebaisse, E. Boni, P. Tortoli, C. Cachard, Noninvasive Young's modulus evaluation of tissues surrounding pulsatile vessels using ultrasound Doppler measurement, IEEE Transactions on Ultrasonics Ferroelectrics and Frequency Control 54 (6) (2007) 1265–1271 (online). Available at: http://www.biomedsearch.com/nih/Noninvasive-Youngs-modulusevaluation-tissues/17571824.html

[41] J. Fromageau, J.-L. Gennisson, C. Schmitt, R.L. Maurice, R. Mongrain, G. Cloutier, Estimation of polyvinyl alcohol cryogel mechanical properties with four ultrasound elastography methods and comparison with gold standard testings, IEEE Transactions on Ultrasonics Ferroelectrics and Frequency Control 54 (3) (2007) 498–509 (online). Available at: http://www.biomedsearch.com/nih/Estimationpolyvinyl-alcohol-cryogel-mechanical/17375819.html

[42] S. Yan, R.S. Witte, M. O'Donnel, Identification of vulnerable atherosclerotic plaque using ivus-based thermal strain imaging, IEEE Transactions on Ultrasonics Ferroelectrics and Frequency Control 52 (5) (2005) 844–850.

[43] E.C. Kyriacou, C. Pattichis, M. Pattichis, C. Loizou, C. Christodoulou, S.K. Kakkos, A. Nicolaides, A review of noninvasive ultrasound image processing methods in the analysis of carotid plaque morphology for the assessment of stroke risk, IEEE Transactions on Information Technology in Biomedicine 14 (July) (2010) 1027–1038 (online). Available at: http://dx.doi.org/10.1109/TITB. 2010.2047649

[44] E. Kyriacou, M.S. Pattichis, C.I. Christodoulou, C.S. Pattichis, S. Kakkos, N. Griffing, A. Nicolaides, Ultrasound imaging in the analysis of carotid plaque morphology for the assessment of stroke, Studies in Health Technology and Informatics 113 (2005) 241–275.

[45] E. Kyriacou, M.S. Pattichis, C.S. Pattichis, A. Mavrommatis, C.I. Christodoulou, S. Kakkos, A. Nicolaides, Classification of atherosclerotic carotid plaques using morphological analysis on ultrasound images, Applied Intelligence 30 (February) (2009) 3–23 (online). Available at: http://portal.acm.org/citation.cfm?id=1485060.1485063

[46] J. Seabra, L.M.P. (MD), F. e Fernandes, J.M. Sanches, Ultrasonographic characterization and identification of symptomatic carotid plaques, in: Engineering in Medicine and Biology Society, 2010. EMBS. 32th Annual International Conference of the IEEE, September, 2010.

[47] R.U. Acharya, O. Faust, A.P. Alvin, S. Vinitha Sree, F. Molinari, L. Saba, A. Nicolaides, J.S.J.S. Suri, Symptomatic vs. asymptomatic plaque classification in carotid ultrasound, Journal of Medical Systems (January) (2011), http://dx.doi.org/10.1007/s10916-010-9645-2.

[48] U.R. Acharya, O. Faust, S.V. Sree, F. Molinari, L. Saba, A. Nicolaides, An accurate and generalized approach to plaque characterization in 346 carotid ultrasound scans, IEEE Transactions on Instrumentation & Measurement 61 (4) (2012) 1045–1053.